Thinned array distribution with grating lobe canceller at any scan angle for automotive radar applications

Masato Kohtani[1] , Sungwoo Cha[1], Paul Schmalenberg[2] , Jae Lee[2] ,
Linjie Li[3], Toshihiko Takahata[1], Shinji Yamaura[1] , Toshihiko Matsuoka[1] and
Gabriel M. Rebeiz[3]

[1]MIRISE Technologies Corporation, Sensor R&D Division, Tokyo, Japan; [2]Toyota Research Institute of North America, Electronics Research Department, MI, USA and [3]University of California, San Diego, CA, USA

Abstract

A novel thinned antenna element distribution for cancelling grating lobes (GLs) as well as for reducing phase shifters (PSs) is presented for a two-dimensional phased-array automotive radar application. First, an efficient clustering technique of vertical adjacent elements is employed with array thinning for a PS reduction of 66.7%. In the proposed distribution, several single-element radiators (non-clustered antenna elements) are placed in the vertical direction with specific spacing in a grid of 16×12 (192) elements with $\lambda/2$ pitch. This disrupts the periodicity of phase-centers after element-clustering and takes a role as steerable GL canceller with capabilities of tracking and nullifying the GL at any scan angle. The proposed distribution enables beam steering up to $\pm 60°$ in the azimuth plane, as well as $\pm 25°$ in the elevation plane with cancelled GL and sidelobes. Furthermore, the proposed distribution has been efficiently calibrated with all elements activated by introducing the code division multiple access technique. To the best of the authors' knowledge, this work represents the first fully calibrated state-of-the-art thinned distribution phased-array including a novel steerable GL canceller to track and nullify GLs.

Introduction

More accurate detection of moving objects with extended range will be required for future Autonomous Driving/Advanced Driver Assistance Systems (AD/ADAS). To realize 360° circumference sensing, multiple radar sensors capable of short, medium, and long-range detection will be required in vehicles [1, 2]. Recently, various multiple-input multiple-output (MIMO) radars composed of many multichannel integrated circuits (ICs) to realize extended virtual receivers (RXs) have been reported. For example, a 4D imaging MIMO radar with as many as 1,728 virtual channels (36 transmitters [TXs] $\times$ 48 RXs) composed of 12$\times$ multichannel radar ICs (3 $\times$ TXs and 4 $\times$ RXs) has been presented in papers [3, 4] for high angular resolution.

In the case of a phased-array imaging radar for an AD/ADAS system, there are strong demands such as (i) long range detection, (ii) narrow beam aiming at high resolution and interferer suppression, (iii) wide field of view (FoV), and (iv) low cost and low power consumption by reducing phase shifters (PSs).

More recently, there has been an increasing focus on the design of phased-arrays with more and more antennas not only for 5G applications but also for imaging radar applications [5, 6]. In effect, a phased-array provides a very efficient way to combine power in space. The improved effective isotropic radiated power and signal-to-noise-ratio of large phased-arrays effectively translate to an improvement in link range. In fact, the link range enhancement using phased-arrays makes it possible to contemplate using long-range Si-based millimeter-wave radios [5]. This approach is categorized as an analogue beam forming by combining many antennas with phased and amplitude-controlled signals, which is a completely different approach from papers [3, 4].

In, for example, a phased-array automotive radar application, a large element count (N), and fine beam steering are indispensable for phased-array based radar performance [6].

$$R_{\max} = \left(\frac{N^3 P_{\mathrm{T}} G_{\mathrm{TX}} G_{\mathrm{RX}} \lambda^2 \sigma}{S_{\min}(4\pi)^3} \right)^{1/4}, \tag{1}$$

where G_{TX} and G_{RX} are antenna gain for TX and RX, respectively, P_T is TX output power, and S_{min} is minimum detectable power. From Equation (1), to enhance maximum range, an increased number of active antenna elements (N) is crucial. N^3 can be expressed by $N_{\text{TX}}^2 {}^* N_{\text{RX}}$, which means that each TX output power does not need to be high if a large number of N_{TX} is chosen. The half-power beamwidth (HPBW, Ω_{BW}) can also be expressed with N as [6, 7]

$$\Omega_{\text{BW}} = 0.886\lambda / (Nd). \qquad (2)$$

where d is the antenna element pitch. In general, the array directivity is proportional to $10\log_{10}(N)$. Therefore, narrowing the beam by increasing N is crucial for long range radar applications.

In paper [4], the high-resolution MIMO radar shows blocker suppression of 11 dB to detect a pedestrian at an intersection representing a weak target in the proximity of a car representing a strong target in an angular domain with the shaped beam and low sidelobe level (SLL) by employing an adaptive TX beamforming capability with integrated TX PSs. The half-power beamwidth is 17° in the elevation plane and 67° in the azimuth plane, respectively. Much more suppression can be expected with a narrower beam of less than 10° and suppressed sidelobe/grating lobe (GL) of less than −30 dBc as a TX-RX round-trip by increasing the number of antenna (N).

A phased-array automotive radar system operating at 79 GHz for collision avoidance and cruise control has been reported in papers [8, 9] for long range detection featuring radio frequency (RF) beamforming capabilities and interferer suppression with low sidelobes. Furthermore, for short-range radar applications, wider FoV (scan angle in this case) tends to be required. According to Yole's report in EuMW2022 [10], FoV requests such as ±60° in azimuth and ± 40° in elevation by 2030 are also extending to accommodate the expected demand for crossing scenarios and suppressing the blind zones. In paper [9], a wide FoV of ±50° scanning capability has been demonstrated for short-range collision-avoidance radars. Also, a unique hybrid radar system to form narrower virtual beams within the real beam has been presented in paper [11] aiming at fast scanning time with optimized beamwidth as well as high angular resolution imaging capability, where the number of RXs is the same as the number of two-dimensional RX subarrays. In such a radar application, wide scanning angle capability is crucial to realize a wide FoV.

In a phased-array design, less complexity by reducing PSs is one of the most challenging requirements. There are two representative approaches regarding a sparsity to realize less complexity in an array [12]. The first approach is a sparse array with individual antenna elements in controls of phase and amplitude. It is possible to remove (or to "thin") several of the elements in an array without significantly changing its beamwidth since the array beamwidth is related to the maximum dimension of the aperture. The array gain for a thinned array will be reduced in approximate proportion to the fraction of elements removed, since the gain is proportional to the active elements [7]. The other approach is an array including subarrays by clustering adjacent elements, where each geometric center (or phase-center) in a subarray is sparsely located. Figure 3 in paper [12] shows an example of an array layout with rod-shaped subarrays of $1 \times X$ ($X = 13, 15, 17,$ and 19) by clustering many elements only in a horizontal direction since the required azimuth range of ±2° is not so stringent compared with ±10° in elevation for a Ka-band synthetic aperture radar application. However, the subarray approach may lead to the occurrence of GLs depending
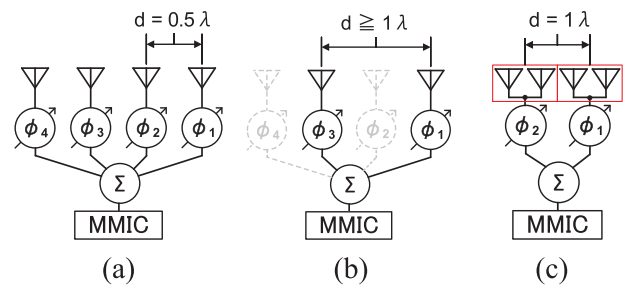
Figure 1. Schematic diagram of phased arrays along with two representative design techniques to reduce phase shifters: (a) conventional array; (b) thinning technique; and (c) clustering technique.

on the subarray distribution, which is explained later in this paper. To achieve grating-lobes-free patterns, a genetic algorithms-based array optimization of irregular subarray layouts with asymmetric polyomino to randomize phase-center pitch in a 40×40 array has been reported in paper [13], which indicates that an increased complexity exists in terms of implementation or modularity of the frontend electronics with PSs and tends to result in no measurements in the paper. The demand of less complexity in a large-scaled array has still been increasing recently.

As shown in Fig. 1, to reduce the number of PSs depicted as ϕ_n, where n is an integer, there are two representative array design techniques such as array thinning for sparsity and clustering techniques in a half-lambda pitch as mentioned above. Monolithic microwave integrated circuit means a multichannel radar IC. The clustering technique is one of the most effective ways since the number of active elements remains the same while the number of PSs can be reduced by a factor of 0.5 at least. As for a two-dimensional large-scaled phased-array design with much wider scanning angles than in paper [12], reducing PS usage has also been researched rigorously for cost reduction, relaxed thermal issues, simplified system design, and reduced control complexity compared with paper [13]. For example, to reduce the PSs by 75% in a 16×16 phased-array at 14 GHz, in-depth research has been reported in paper [14] focusing on better sidelobes with randomly clustered subarray techniques representing scanning capability of ±40° in azimuth and ±15° in elevation. In a similar way, a 16×16 phased-array at 73 GHz for E-band communication link featuring clustering of eight adjacent elements (4×2 or 8×1) to disrupt the periodicity of the phase-shift center for GL cancellation has been reported in paper [15], whose design approach can be categorized as an off-grid random pitch design on X-Y coordinates. Paper [15] shows a narrow scan angle of less than 10° limited by a strong GL of −9 dBc. In this method, the approach of clustering elements in pursuit of reducing PS usage results in narrower scan angles mainly caused by GL issues.

To investigate the GL issue in the case of vertically clustered elements, an ideal 16×12 uniform rectangular array (URA) with $\lambda/2$ pitch was analyzed as shown in Fig. 2. By clustering vertical adjacent elements with the shared phase-shift values calculated as an average phase of the shared elements as in Fig. 2 (left), PS usage can be reduced by half while keeping the array directivity. But once the vertical clustering of adjacent elements is applied, GL will appear easily in the visible region as shown in Fig. 2 (right) even for an ideal URA since the phase-center pitch doubles after clustering. Therefore, a GL cancellation technique is required if the clustering method for reduced PS is applied to any array distribution.
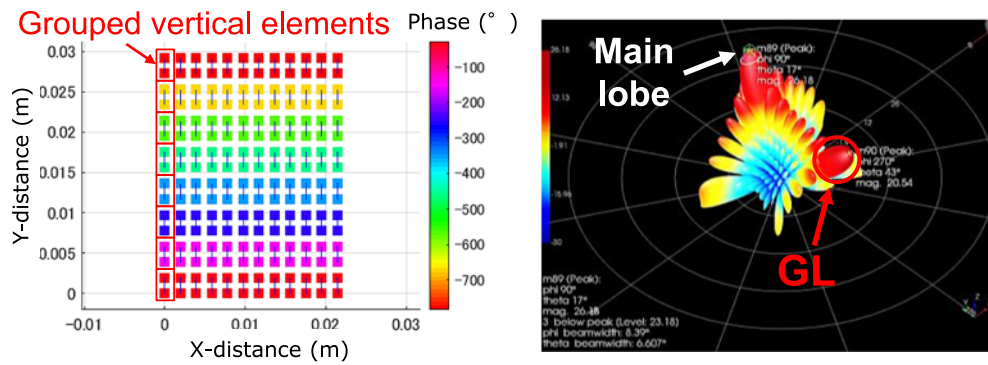
Figure 2. 100% URA as a reference with vertically clustered elements (left) and the simulated 3D beam pattern steered at 17.5° in the elevation plane (right).
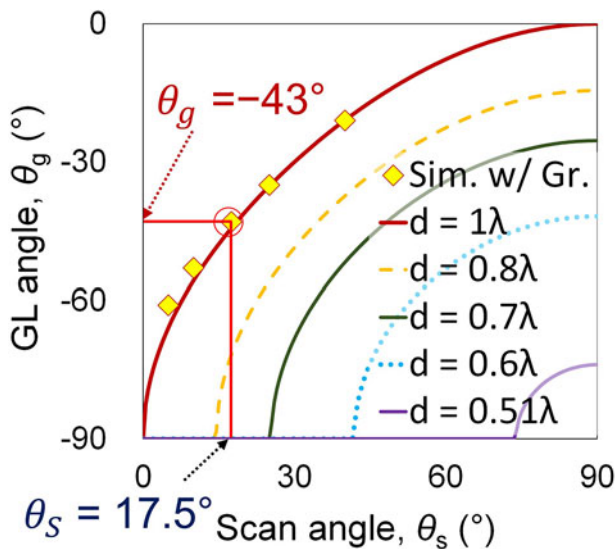

Figure 3. The theoretical analysis on GL angle vs. scan angle plotted with vertically clustered array.

Based on a classical phased-array theory, GL angle (θ_g) is expressed as [16]

$$\theta_g = \sin^{-1}\left(\sin\theta_S - \frac{\lambda}{d}\right), \tag{3}$$

where θ_S is the scan angle. Equation (3) indicates that GL angle changes depending on scan angle as shown in Fig. 3. The simulated grating angle for a 100% fully populated array as in Fig. 2(a) with vertical clustering is plotted with diamond symbols, which shows good agreement with the theoretical plot in the case of $d = 1\lambda$. From Equation (3), if a scan angle is steered at 17.5° in elevation, GL appears at −43°, which could cause false detection by the radar. The larger the scan angle becomes, the closer the GL angle comes near the boresight in the required FoV. GL energy becomes strong especially within a FoV for which it is difficult to mitigate GL since enough gain exists in terms of antenna element gain. Therefore, it is desirable that GL should be suppressed at any scan angle when reducing PSs.

The proposed array distribution includes the two design techniques of thinning for sparsity and clustering elements mentioned above. Besides, a novel GL canceller composed by non-clustered single-element radiators is implemented in an array. Figure 4 represents the basic concept of the proposed GL cancellation

methodology with a GL canceller featuring several single-element radiators with specific spacing to nullify and track GL for the proposed distribution. As shown in Fig. 4b, the null angle is controlled to always align with the GL angle as shown in Fig. 4a to cancel the GL while the main lobe is not attenuated. The resultant beam pattern with GL canceller is shown in Fig. 4c steered at 17.5° in elevation with controlled phase shifts as shown in Fig. 4d.

In order to verify the proposed unique distribution idea with single-element radiators, a 28 GHz 5 G demonstrator with 256 elements reported in paper [17] was utilized. Also, an advanced code-base calibration for the proposed distribution was performed with the efficient code division multiple access (CDMA) technique reported in paper [18].

A novel thinned antenna element distribution aiming at cancelling GLs as well as for reducing PSs was initially presented at EuMW2022 in pursuit of a two-dimensional phased-array automotive radar application [19]. This paper presents a novel phased-array with (i) reduced PS usage of less than 1/3, (ii) wide scan angles of azimuth of ±60° and elevation of ± 17.5°, and (iii) no GL at any scan angle at any frequency while maintaining a good level of regularity and modularity without any GL over wide scanning range. In-depth analysis on the GL canceller is described with theoretical analysis, and a TX*RX codesign approach is additionally explained in search of much better sidelobe performance in two-dimensional arrays, which is regarded as an extension of what has been reported in our previous works [19].

This paper is organized as follows: First, in the "Design of a thinned array with GL cancellers" section, the design of the proposed arrays is described in detail with theoretical considerations. The measurement results are shown in the "Measured results" section, and the advanced design of the TX*RX codesign is described in the "TX*RX codesign of arrays" section, while the conclusion is given in the "Conclusion" section.

Design of a thinned array with GL cancellers

An array distribution can be optimized through hundreds of MonteCarlo simulations so that an array distribution can comply with basic performances including directivity and SLLs of less than −15 dBc under the severe conditions in scanning horizontally at 60° and vertically at 17.5°, for example. Clustering technique of two-adjacent elements only in the vertical direction to reduce PSs by a factor of 0.5 since a vertical scanning range requirement is not so stringent compared with a horizontal one. The occurrence of GLs can be expected only in scanning vertically because of the
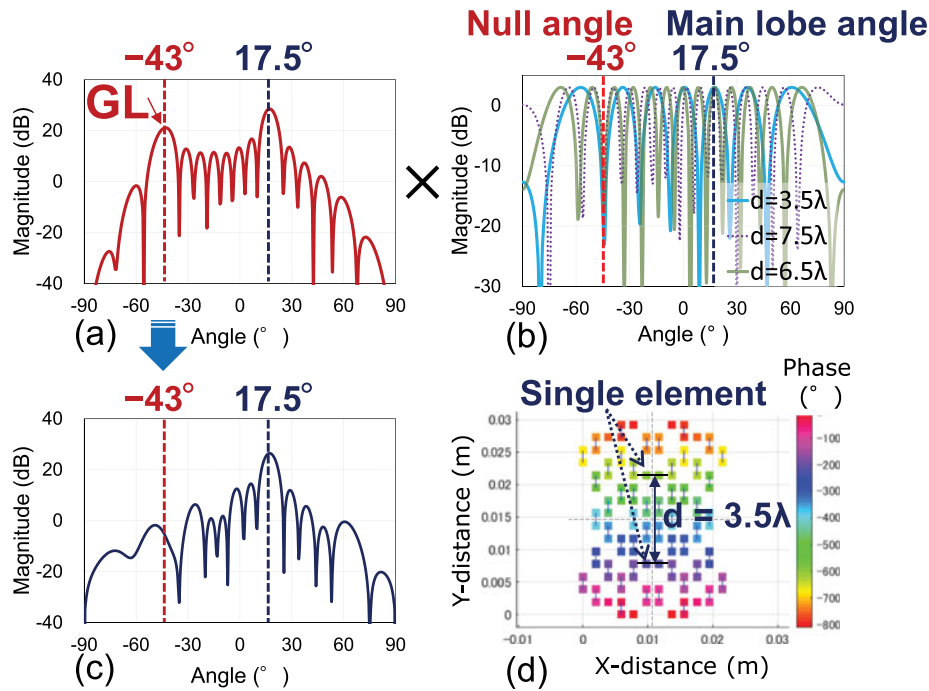
Figure 4. Concept of the proposed GL suppression methodology at 17.5° vertical scan: (a) beam pattern in the elevation plane for reference array with GL caused by vertical clustering; (b) simulated three types of GL canceller steered at 17.5° to create nulls at GL angle; (c) the beam pattern to show GL cancellation due to GL canceller; and (d) the proposed distribution including single-element radiators with spacing of $d = 3.5\lambda$ and so on for GL cancellation along with color maps to elaborate the shared phase-shift values on clustered elements.

1λ phase-center pitch vertically. So, the proposed GL canceller was designed to suppress GL especially in vertical scanning. A point-symmetric design was employed as well, which enables a mirrored design with $4 \times$ quadrants copied from one quadrant in an array, which can be beneficial to save time in an array design and to reuse layout routings connected to PSs.

Steerable nulls for GL cancellation

Figure 5 depicts the key design techniques of the proposed wave-like distribution in a half-lambda grid such as (i) single-element
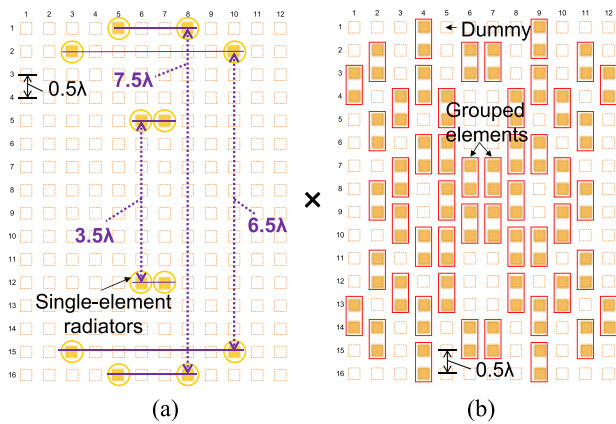
Figure 5. The breakdown of the proposed 16 × 12 wavelike distribution: (a) single-element radiators with specific spacing for GL cancellation; (b) vertically clustered elements after array thinning for sparsity.
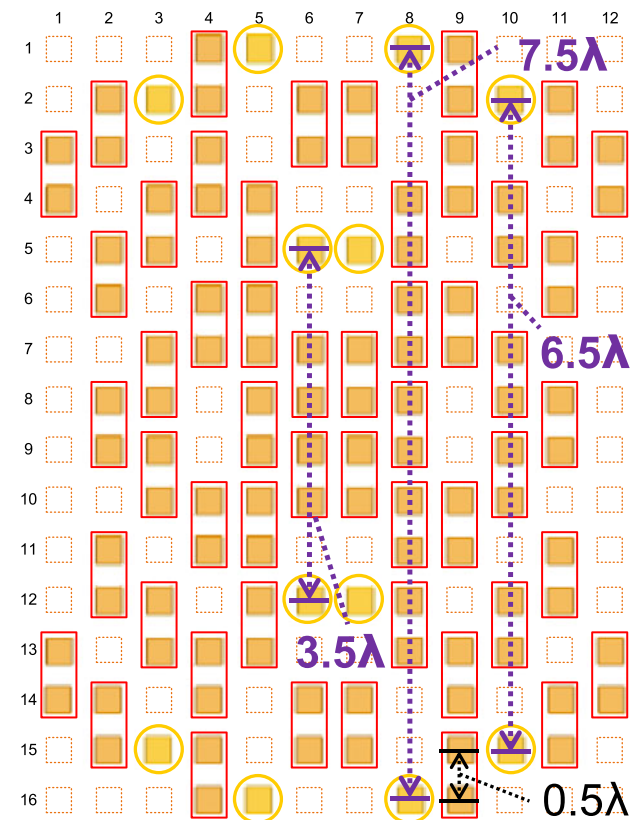
Figure 6. The proposed 16 × 12 wavelike distribution including single-element radiators with specific spacing for GL suppression.

radiators with specific spacing for GL cancellation, (ii) vertical clustering of two adjacent elements to reduce PSs, and (iii) array thinning for sparsity. A novel array distribution was created by superposition of the key techniques in the same array area of 16×12.

Figure 6 presents the proposed point-symmetric wavelike distribution including three types of steerable GL canceller with different spacing to strengthen the filtering capabilities. In order to realize steerable null functionalities as a GL canceller, several single-element radiators (non-clustered antenna elements) are placed within some columns of the array with different spacing as shown in Fig. 5(a) expressed as

$$d = [0.5 + (2 \times 0.5 \times m)] \times \lambda = (0.5 + m) \times \lambda, \quad (4)$$

where m is an integer ($m = 1, 2, \cdots$), which corresponds to $(2m + 1) \times \lambda/2$, a spacing of half-lambda multiplied by odd number. Also, the embedded null patterns are beneficial not only to disrupt the periodicity between distant phase-centers caused by the vertical clustering but also to take a role as steerable GL canceller with capabilities of tracking and nullifying GL at any beam steering angle.

Thinned array design

To reduce the number of PSs, clustering elements is one of the most efficient approaches. For example, if two-thirds of the elements, 128 elements (66.7%), are randomly activated among the 192 elements in a 16×12 array, a PS usage of 33% can be achieved through vertical clustering of two adjacent elements, which requires 64 PSs. The array directivity is maintained by employing the clustering approach in the vertical direction. In Fig. 6, the distribution of 116 active elements including 12 single-element radiators and 104 clustered-elements as shown in Fig. 5(b) were controlled by keeping high density at the center with "$m \geqq 3$" in Equation (4) for better SLLs, which still complies with the reduced number of 64 PSs after clustering. Monte Carlo simulation for element failure tests is helpful to screen out several low-priority elements as many as possible complying with SLL requirements, where active elements tend to be optimized to be located as high density at center and low density at a corner for better SLLs as shown in paper [13]. Several clustered elements were removed (or thinned) to meet 66.7% reduction of PSs. Besides, some of the clustered elements can be relocated by shifting upward or downward in a vertical direction so that a symmetrical radial pattern can be formed as shown in Fig. 5(b) for balanced scanning performances. Finally, total 64 IDs among active elements are assigned for clustered elements and single-element radiators, which will be connected to 64 PSs. Figure 7 represents the simulated GL cancellation capability due to the proposed steerable null characteristics, where the main beam was steered at 5°, 17.5°, 25°, and 40° in the elevation plane, compared with the 100% reference array with vertical clustering of adjacent elements as shown in Fig. 2(left). The GL canceller with $d = 3.5\lambda$, 6.5λ, and 7.5λ were implemented for the proposed wavelike distribution. Regarding single-element radiators in Fig. 6, minimum distance of 3.5λ was carefully designed at around center, which will be effective to get the GLs and zeroes to overlap. The other distance of 6.5λ and 7.5λ were chosen to keep better SLLs. Note that no tapering is applied in this simulation. As mentioned in the "Introduction" section, the GL angle comes near the boresight direction with remaining strong energy as the scan angle becomes large as shown in Fig. 3 based on Equation (3), which causes false detection in a radar. On the other hand, the steerable null angle in
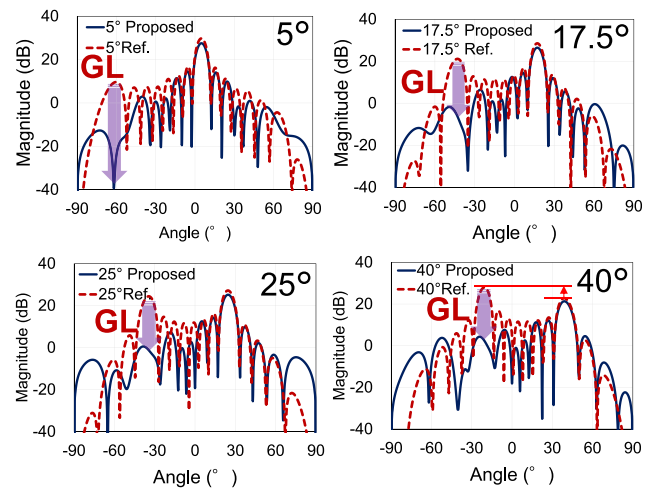

Figure 7. Simulated beam comparison between 100% reference array in Figure 1 with vertical clustering and the proposed wavelike distribution at 5°, 17.5°, 25°, and 40° in the E-plane after clustering without any tapering.

the proposed array distribution is always tracking and nullifying the GL observed at −61°, −43°, −35°, and −21°, respectively. Seen from Fig. 7, a GL cancellation of over 15 dB at any scan angle is achieved due to the GL canceller.

Directivity considerations in a thinned array

In general, as many elements as possible should be activated for best directivity. In an effort to achieve 33% (=64/192) PS usage and to tackle the GL issue simultaneously, an active elements ratio of 60.4% (116 elements) including single-element radiators was optimized for the proposed wavelike distribution as shown in Fig. 6. The array directivity at broadside except antenna loss can be estimated from the total number of activated elements as

$$D_{\text{array}} = 10\log_{10}\left(16 \times 12 \times 60.4\%\right) + D_{\text{element}} = 20.6 + 5.5$$
$$= 26.1 \text{ dB}. \quad (5)$$

For example, compared to the aforementioned 66.7% reference design without the single-element radiators, a penalty of 0.4 dB for GL cancellation can be estimated from Equation (5). Namely as small as 12 single-element radiators, which corresponds to 18.8% among 116 active elements, were dedicated to cancel GL as well as to minimize directivity loss. In the simulation, the proposed wavelike distribution results in a TX*RX round-trip SLL of better than −40 dBc at broadside with −7 dB raised cosine tapering.

Phased-array factor in theory

In general, the phased-array factor for a conventional uniform linear array (ULA) as shown in Fig. 8 is expressed as [20]

$$\text{AF}(\theta) = \sum_{n=1}^{N} A_n e^{j(n-1)\left(-\frac{2\pi}{\lambda} d_{\text{u}} \sin\theta + \beta\right)}, \quad (6)$$

where β is the phase term, which can be expressed as $\frac{2\pi}{\lambda} d_{\text{u}} \sin\theta_{\text{S}}$. θ_{s} is the scan angle. The part $-\frac{2\pi}{\lambda} d_{\text{u}} \sin\theta$ is regarded as a geometry term. θ is a kind of a twiddle factor with a search range from
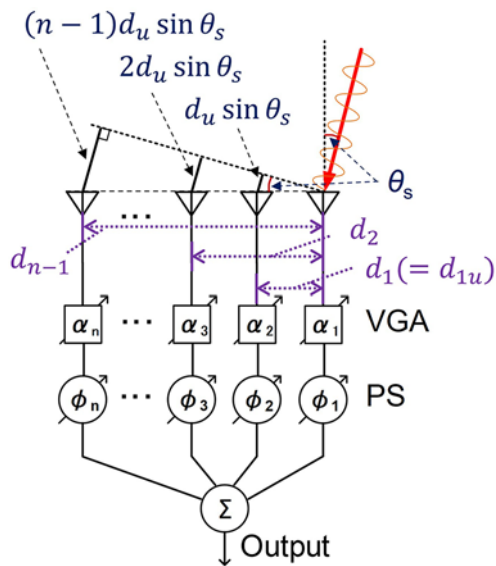
Figure 8. Schematic drawing of a conventional ULA.

−90° to 90°. Amplitude weight (A_n) can be controlled by a variable gain amplifier (VGA). d_u is the unit of element pitch of 0.5λ.

Phased-array factor with clustering in theory

The phased-array factor by employing vertically adjacent clustered elements as shown in Fig. 9 which corresponds to Fig. 5(b) is expressed as

$$\mathrm{AF}_2(\theta) = \sum_{n=1}^{N} A_n e^{j(n-1)\left(-\frac{2\pi}{\lambda} 2d_u \sin\theta + \beta\right)}, \tag{7}$$

where β is the phase term expressed as $\frac{2\pi}{\lambda} 2d_u \sin\theta_S$ in the same manner as in Equation (6). The root cause of the GL issue in reducing PSs is the doubled phase-center pitch of 1λ ($d_1 = 2 \times d_u = 2 \times 0.5\lambda = 1\lambda$) instead of 0.5λ.
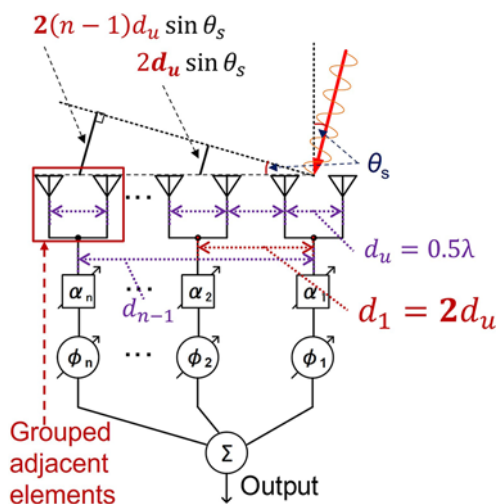

Figure 9. Schematic drawing of a conventional ULA with vertical clustering of two adjacent elements.

The proposed GL canceller in theory

The phased-array factor on single-element radiators as shown in Fig. 10 which corresponds to Fig. 5(a) is expressed as

$$\mathrm{AF}_S(\theta) \propto \sum_{m} \sum_{n=1}^{2} A_n e^{j(n-1)\left(-\frac{2\pi}{\lambda} d_s \sin\theta + \beta\right)}. \tag{8}$$

It is crucial that single-element radiators should be placed with specific spacing of $d_s = (m + 0.5)\lambda$ where $m = 3, 6$, and 7 in this design to create null at GL angles for GL cancellation. As shown in Fig. 11 in the case of $d_s = 3.5\lambda$, the simulation says that the null angle is controlled to align with the GL angle as expected while the main lobe is not attenuated. The steerable GL cancellers are essential to track and cancel GL. A different pitch of $d_s = 6.5\lambda$ or $d_s = 7.5\lambda$ creates different filtering characteristics as shown in Fig. 4(b) to strengthen the filter characteristics for GL cancellation.

In this way, two different mechanisms consisting of single-element radiators with specific spacing and vertically clustered
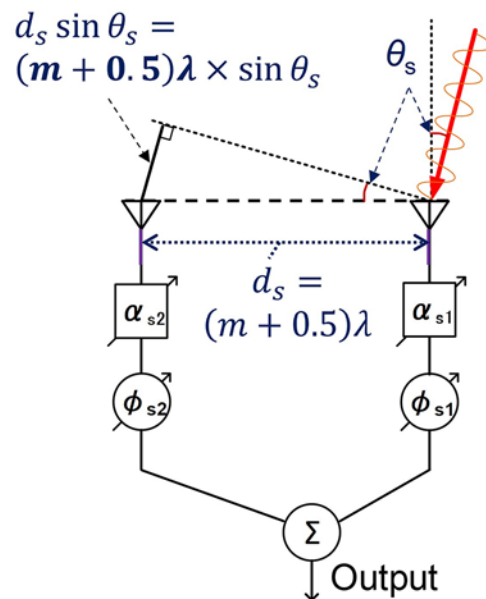

Figure 10. Schematic drawing of the proposed single-element radiators for GL cancellation.
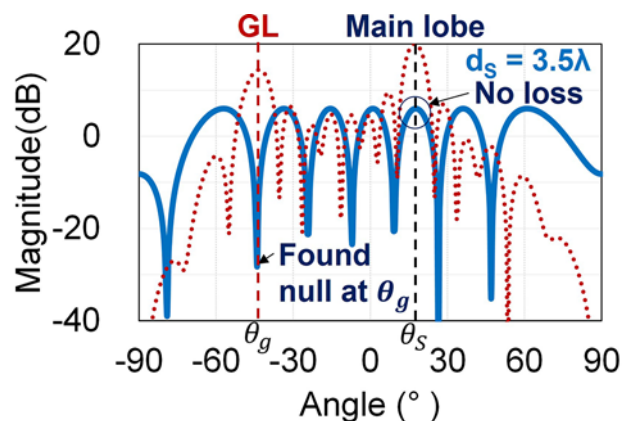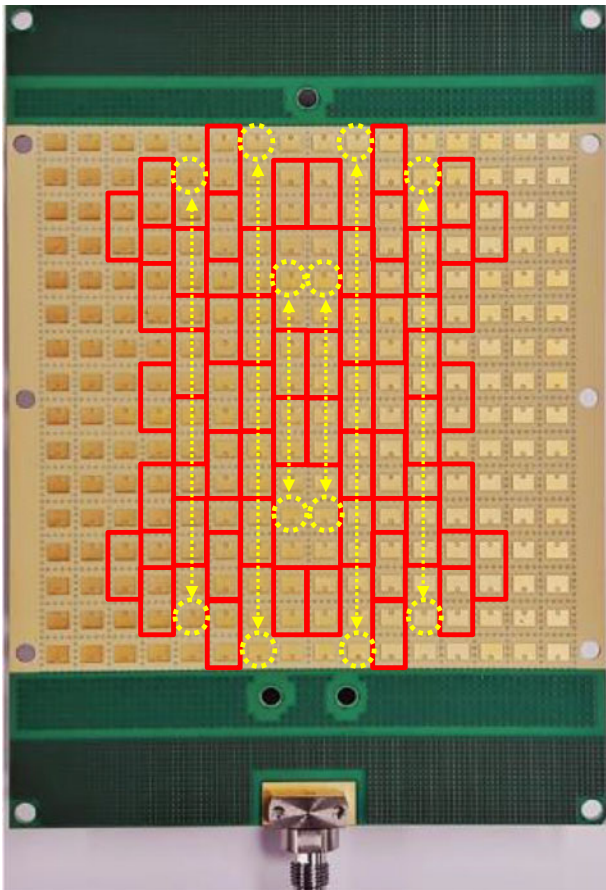

Figure 11. The simulated principle of the proposed GL canceller for the proposed single-element radiators in the case of the distance of $d_s = 3.5\lambda$.

Figure 12. Activated elements with red boxes and yellow circles for the proposed wavelike distribution with 116 active elements mapped on the 16 × 16 URA [15].
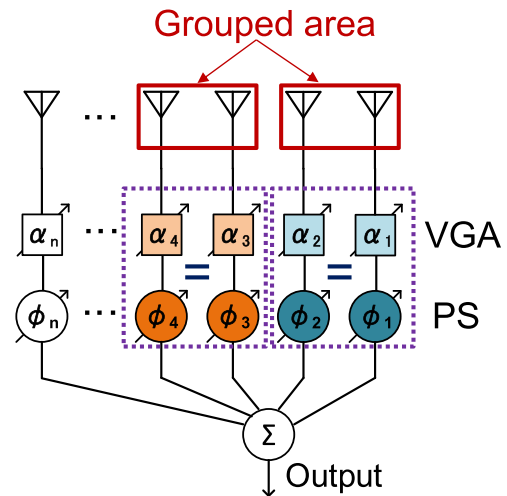

Figure 13. Schematic drawing of array with vertical clustering of two adjacent elements in Figure 12.

Figure 14. The proposed symmetry array distribution and random array as a reference with the same PS usage of 33%.
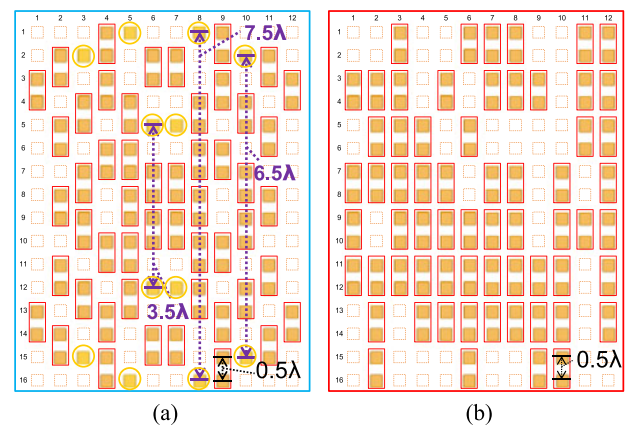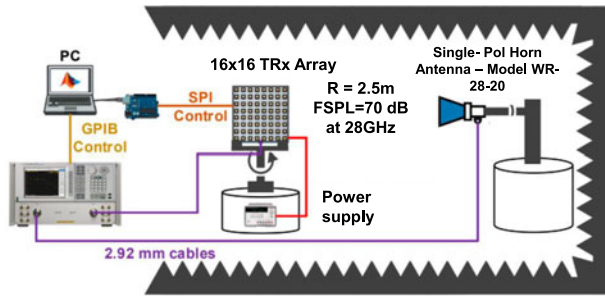
Measured results

The proposed distribution with 116 active elements was mapped onto a 256-element array [16] as shown in Fig. 12, where each element is connected to a PS as shown in Fig. 13. The phase (ϕ_n) and amplitude (α_n) of the 116 active elements are controlled by the corresponding PSs (T/R modules). On the other hand, the PSs (T/R modules) connected to the remaining non-active elements are turned off. Since there is a T/R module on every element, phase and amplitude were set the same for the two vertical antennas in the red box in Fig. 13 to form a vertical element clustering structure. All the remaining elements were deactivated as a dummy as shown in Fig. 12. The – 7 dB raised cosine tapering was implemented in the proposed array controlled with VGA to minimize sidelobes near the main lobe.

Two array designs for comparison

For comparison purposes, two array distributions were designed on a half-lambda grid with the same PS usage of 33% as shown in Fig. 14. Two array design techniques of clustering and array-thinning for sparsity were applied to both arrays. For the proposed array, single-element radiators with $d_s = (m + 0.5)\lambda$ as in Equation (4), where $m = 3$, 6, and 7, were implemented and the

number of active elements (N_{ON}) were 116 counts including single-element radiators and clustered elements out of the 192 ($=16 \times 12$) elements as shown in Fig. 14(a). Finally, 64 PSs in total were used, which corresponds to 33% PS usage. Note that if the number of active antenna elements were 64 counts instead of 116 without any clustering (each antenna is connected to each PS), directivity loss would be greater than 2.5 dB and a GL issue would be a concern again with the extended pitch of the antenna array elements.

On the other hand, the random array was optimized using Monte Carlo simulation focusing on better sidelobe performance, and the number of active elements (N_{ON}) were 128 counts out of 192 elements as shown in Fig. 14(b). Totally, 64 PSs were used, which corresponds to the same PS usage of 33 % as the proposed array.

Measurement setup

The measurement setup is shown in Fig. 15, where the range was set to 2.5 m with free space path loss of 70 dB at 28 GHz as shown in paper [17]. Calibration and beam pattern measurements for the proposed 116 elements were performed at 27 and 28 GHz, respectively. The two kinds of measurements were performed by

elements after array thinning for sparsity are overlaid or co-exist in the proposed wavelike distribution which leads to GL cancellation.

Figure 15. Measurement setup of calibration and beam patterns at a distance of 2.5 m for the proposed 16 × 12 wavelike distribution.

Figure 17. Measured vs. simulated comparison of 28 GHz beam patterns at 25° in the E-plane for the proposed wavelike distribution along with the thinned reference array as shown in Figure 14(b).
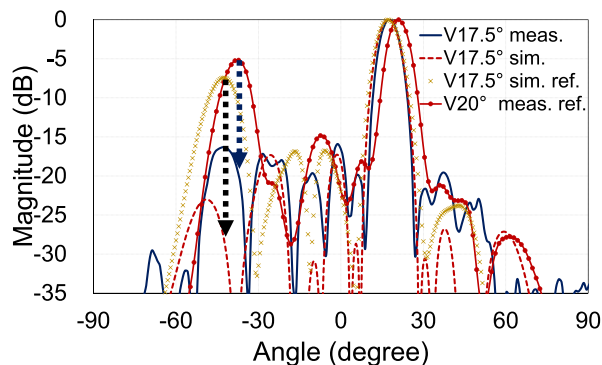
employing a network analyzer: (i) phase and amplitude calibration focusing on S21 for TX and S12 for RX at boresight condition and (ii) beam pattern measurement with the rotator within ±90°.
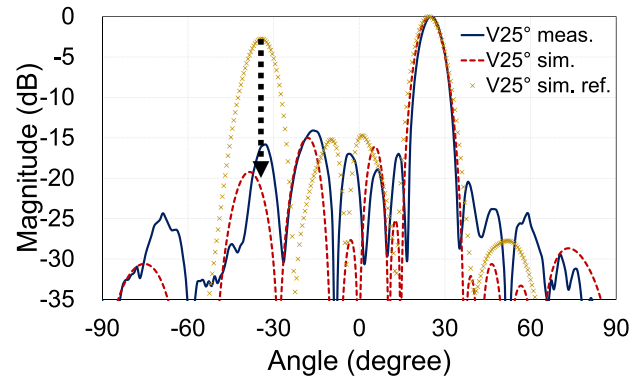
Code-base calibration for the proposed distribution

Advanced code-base calibration was performed by monitoring S21 with a KEYSIGHT N5245B PNA-X 50 GHz network analyzer for the proposed distribution with 116 active elements, which is regarded as a remarkable extension of what has been reported in paper [18]. It was proved that any array including the proposed wavelike distribution can be calibrated flexibly and efficiently with the CDMA code-base calibration. In the CDMA calibration, the effect of temperature and mutual coupling are taken into account with all necessary elements activated. The code length of 128 (2^7), which corresponds to 116 active elements and 12 ideal dummies, was utilized since the rank of Walsh matrix can only be 2^{N*2^N} ($N = 7$). The resultant root mean square phase error of around 6° and amplitude error of around 0.7 dB at 28 GHz were achieved as expected and was limited by the performance of the PSs.

GL cancellation capabilities

Figure 16 shows the measured and simulated beam pattern comparison at 17.5° in the elevation plane (E-plane), also plotted with the measured 20° in the E-plane for the conventional reference array at 28 GHz as shown in Fig. 14(b), while Fig. 17 shows measured and simulated beam patterns at 25° in the E-plane. In the case

of 17.5° in the E-plane as a target maximum scan angle, GL was successfully cancelled by 12 dB in the measurement. Note that a −7 dB raised cosine tapering and an antenna element factor of $\cos^{1.2}(\theta)$ were applied in both the simulation and the measurement.

RF beam scanning capabilities

Figure 18 shows the measured results in the E-plane at 28 GHz with different scan angles of −17.5°, −10°, −5°, 0°, 5°, 10°, and 17.5° along with the extreme conditions of −40°, −25°, 25°, and 40°. The measured peak sidelobes of −16.4 dBc at 17.5° in the E-plane and −14.4 dBc at 25° in the E-plane were achieved, respectively, which corresponds to better than −32.8 dBc at 17.5° in the E-plane expressed in the TX*RX (Now TX = RX) round-trip beam calculation. It was proved that GL has been cancelled in the E-plane due to the insertion of the single-element radiators with specific spacing even after vertical clustering of adjacent elements for the proposed wavelike distribution. Although the element pitch was 0.53λ for the 28 GHz demonstrator as in Table 1, GL cancellation has been confirmed. Also, a massively reduced number of elements were achieved while still narrow beamwidths and low SLLs were maintained. Figure 19 shows the measured results in the azimuth plane (H-plane) at 28 GHz with different scan angles from −60° to 60° with a 15° step. There is no GL in the H-plane as expected since the λ/2 element
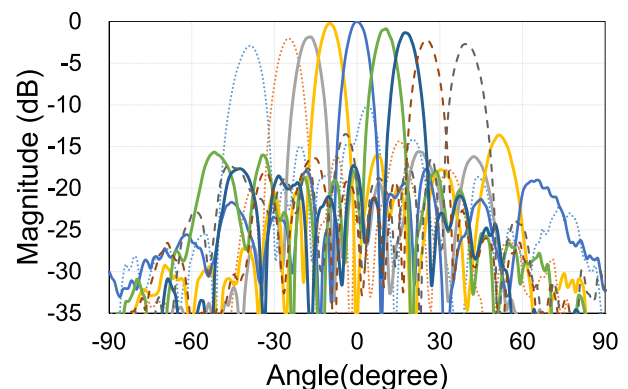

Figure 16. Measured vs. simulated comparison of 28 GHz beam patterns at 17.5° in the E-plane for the proposed wavelike distribution along with the thinned reference array measured at 20° as shown in Figure 14(b).

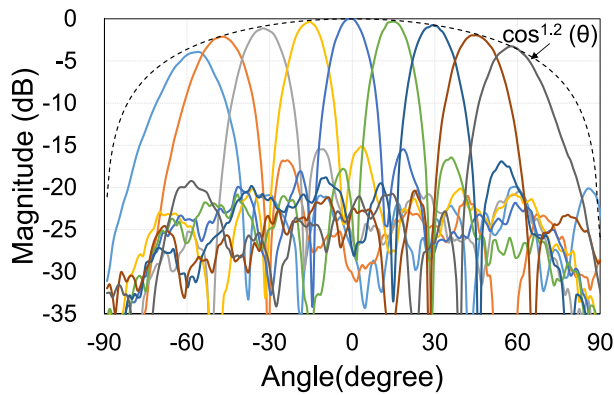**Figure 18.** Measured beam patterns in the E-plane results at 28 GHz for the proposed wavelike distribution from −40° to 40°.

Table 1. Measured and simulated beamwidth for the proposed distribution

16 × 12 array	Ω_{BW}_(H-plane)	Ω_{BW} (E-plane)	H-pitch design	V-pitch design
Simulation	11.1°	7.8°	0.50λ	0.50λ
Meas. at 28 GHz	11.3°	7.2°	0.49λ	0.53λ
Meas. at 27 GHz	11.4°	7.8°	0.47λ	0.51λ
Simulated TX*RX	8.0°	5.8°	0.50λ	0.50λ

Figure 19. Measured beam patterns in the H-plane at 28 GHz for the proposed wavelike distribution from −60° to 60° with a 15° step.

pitch was designed without any horizontal clustering of adjacent elements. The simulated and measured beamwidths show good agreement and are summarized in Table 1. The beamwidth calculated as the TX*RX round-trip (TX distribution is the same as RX) at 17.5° in the E-plane is 5.8° in the E-plane and 8° in the H-plane, respectively, which is estimated from the beamwidth of the RX distribution (Ω_{BW_RX}) multiplied by $1/\sqrt{2}$. Several beam scanning performances such as steerable scan angles are summarized in Table 2.
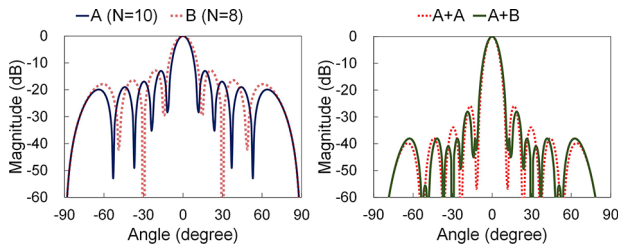
TX*RX codesign of arrays

The TX*RX codesign approach such that new TX distribution is complementarily designed based on the proposed RX distribution in Fig. 6 would be beneficial aiming at additional mitigation of off-axis sidelobes in a two-dimensional phased-array.

Concept of TX*RX codesign for much better SLLs

The number of sidelobes in the H-plane or E-plane can be estimated from $N − 2$ in a row or column as a function of active elements (N) as shown in Fig. 20 (left). For example, if a ULA with $N = 10$ is named as design-A, eight sidelobes appear in solid blue while a ULA with $N = 8$ is named as design-B, six sidelobes appear in dashed red. The combined beam pattern expressed as "A + B" with different arrays in green in Fig. 20 (right) shows better sidelobe performance by a couple of dB compared to "A + A" with the red dotted plot. Therefore, if a TX array is codesigned based on an RX array or vice versa, better sidelobe performance can be expected.

TX*RX codesign with single-element radiators

Much improved SLL can be achieved by employing the TX*RX codesign approach even with the steerable GL canceller as shown in Fig. 21. TX array distribution in Fig. 21(b) was complementarily designed based on the proposed RX array distribution in Fig. 21(a). The proposed GL cancellers were complied with $d_s = (m + 0.5)\lambda$ to strengthen filter responses with $m = 3$, 6, and 7 for RX while $m = 2$, 5, and 7 were employed for TX. As shown in Fig. 21, N_{H_RX} is 8 while $N_{H−TX}$ is 10 in the middle row. The TX*RX codesign concept is depicted in Fig. 22. Figure 23(a) represents $TX \cup RX$ as an overlapped area calculated from Fig. 21 for TX and RX array distributions. In the two-dimensional TX*RX codesign, maximizing $TX \cup RX$ is important for better SLL. The array coverage of active elements in a 16 × 12 array for TX and RX reaches 85.4% due to the complementarily-designed approach compared with the original array coverage of 60.4% in the case that the same array distribution is applied to TX and RX.

Table 2. Performance comparison summary on a beam scan capability

	Target	This work	[14]	[15]
Number of active elements	128	116 on 192 (=16×12)	256 (=16×16)	256 (=16×16)
Number of clustered elements	2	2 (2 × 1 vertically) w/ single-elements	8 (4 × 2, 8 × 1 Va/Hb)	8 (4 × 2, 8 × 1 V/H)
Steerable scan angles	±60° H-plane ±17.5° E-plane	±60° H-plane ±40° E-plane	±40° Az. ±15° El.	±15° Az. ±15° El.
Frequency	28/77 GHz	28 GHz (Meas.) 28/77 GHz (Sim.)	14 GHz	73 GHz
Array design technique	Thinning & clustering	Thinning & clustering	Clustering only	Clustering only
Phase shifter usage[c]	33% (=64/192)	33% (=64/192)	12.5% (=32/256)	12.5% (=32/256)
GL/Sidelobe at large scan angle	−15.0 dBc	−16.4 dBc at 17.5° El. −14.4 dBc at 25° El. −11.0 dBc at 40° El. without GL	−12.0 dBc at 15° El.	−9.0 dBc at 15° El. from graph (GL exists)

[a]Vertical.
[b]Horizontal.
[c]Smaller is better with GL cancellation.

Figure 20. Theoretical comparison of combined beam patterns calculated from *design-A* ($N = 10$) or *design-B* ($N = 8$).

(a) RX   (b) TX
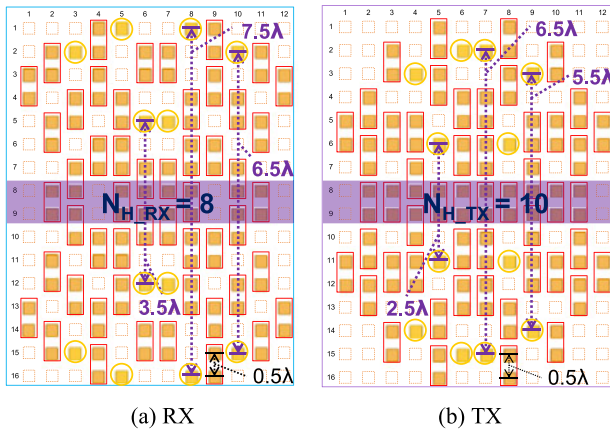
Figure 21. The proposed RX array as a base design with GL canceller ($m = 3, 6,$ and 7) and codesigned TX array with GL canceller ($m = 2, 5,$ and 6) based on an RX array.
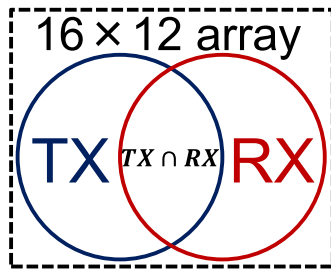

Figure 22. TX*RX codesign concept with Venn diagram.

The area of TX $\cup$ RX in Fig. 22 can also be expressed as TX $\cup$ RX = TX $\cap$ RX + TX $\oplus$ RX in a two-dimensional phased-array as shown in Fig. 23(b), the overlapped area used in both TX and RX arrays, expressed as *TX∩RX*, was designed symmetrically and radiately to achieve better sidelobes in any direction. The corner antenna elements far away from the center can always be removed in a URA since the gain at the corner will be set low concentrically in an array, which is controlled by VGA when applying a tapering.

### Simulated beam pattern for the TX*RX array

The TRX round-trip sidelobe target is below -40 dBc at boresight condition. As shown in Fig. 24, the simulated SLL is better than -58 dBc in the H-plane in Fig. 24(b) which corresponds to an 11 dB improvement originating from -47 dBc in Fig. 24(a) due to the TX*RX codesign. In this way, a different number of SLs (nulls) will help to clean up the remaining sidelobes in a two-dimensional phased-array as shown in Fig. 25. The combined
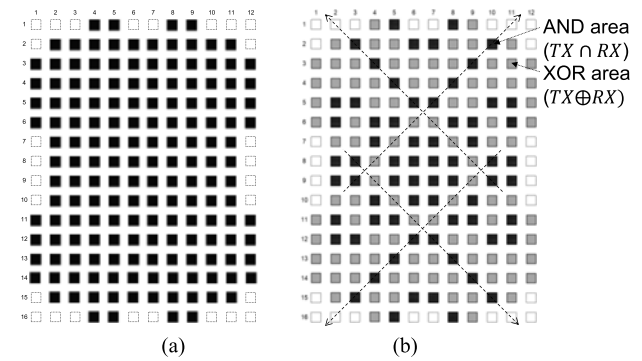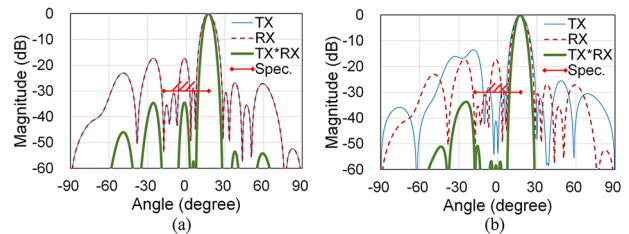

Figure 23. Detailed analysis of TX*RX overlap area analysis of Figure 21: (a) *TX∪RX*; (b) *TX∩RX* and *TX⊕RX*.
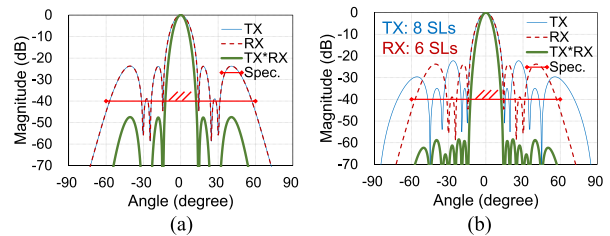
Figure 24. Simulated comparison of TX*RX beam patterns comparing each TX and RX beam pattern at boresight in the H-plane: (a) TX = RX; (b) TX ≠ RX.
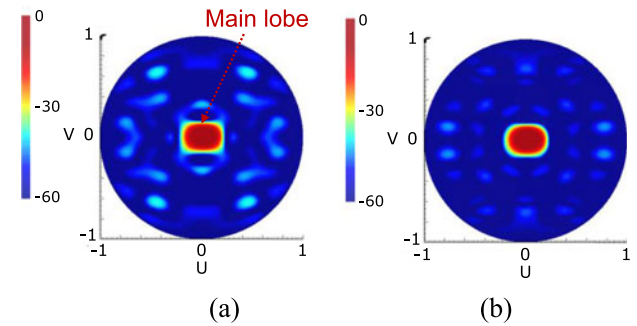
Figure 25. Simulated U-V plot comparison of TX*RX beam patterns at boresight: (a) TX = RX; (b) TX ≠ RX.

Figure 26. Simulated comparison of TX*RX combined beam patterns comparing each TX and RX beam pattern at 17.5° in the E-plane: (a) TX = RX; (b) TX ≠ RX.

TX*RX beamwidths were 8.0° in the H-plane and 5.8° in the H-plane, respectively.

The TRX round-trip sidelobe target is below -30 dBc at steered angles as shown in Fig. 26. The resultant off-axis SLL is better than -31.3 dBc at around bottom left or right in the diagonal direction in Fig. 27(b), which corresponds to 6.6 dB improvement
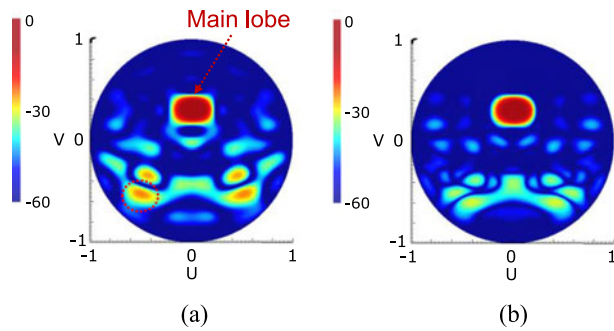
Figure 27. Simulated U-V plot comparison of TX*RX combined beam patterns vertically steered at 17.5°: (a) TX = RX; (b) TX ≠ RX.
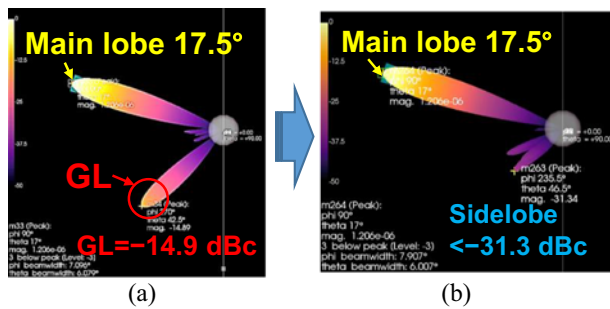
Figure 28. Simulated TX*RX round-trip 3D beam pattern comparison in the condition of vertically steered at 17.5°: (a) Conventional array with vertical clustering; (b) TX*RX codesign with GL canceller.

originating from −24.7 dBc in Fig. 27(a) by TX*RX codesign in a two-dimensional phased-array as shown in Fig. 27 highlighted with a red dashed circle.

In this section, it is revealed that the TX*RX codesign will lead to much improved sidelobe performance. Note that the GL was cancelled for both TX and RX arrays due to the proposed GL canceller. The proposed codesigned TX/RX array distributions are suitable for a future hybrid radar architecture with multiple RX channels as shown in paper [11] accompanied by a single multichannel radar IC, where the number of RXs is the same as the number of subarrays.

3D beam pattern analysis for TX*RX codesign with GL canceller

Finally, a simulated TX*RX round-trip 3D beam pattern comparison between the proposed wavelike distribution in Fig. 14(a) and a conventional random array as a reference such as Fig. 14(b) was performed as shown in Fig. 28. The result of Fig. 28(b) is equivalent to the analysis of Fig. 27(b). GL energy was successfully cancelled by much more than 15 dB compared with the conventional one due to the proposed GL canceller by employing single-element radiators with specific spacing. Furthermore, the off-axis sidelobe was suppressed due to the TX*RX codesign with an SLL of −31.3 dBc as mentioned above. The TX*RX round-trip HPBW steered at 17.5° vertically were 7.9° in the H-plane and 6.0° in the E-plane, respectively.

Conclusion

This paper presents a unique array distribution with steerable GL canceller for GL cancellation. The proposed wavelike distribution

with GL canceller makes it possible to track and nullify GL at any scan angle as well as at any frequency. Both reduced PS usage of 33% after clustering of vertical elements and wide scan angles with small sidelobes were achieved, which will be suitable for phased-array automotive radar systems or point-to-point communication systems in pursuit of low power consumption.

References

1. **Hasch J, Topak E, Schnabel R, Zwick T, Weigel R and Waldschmidt C** (2012) Millimeter-wave technology for automotive radar sensors in the 77GHz frequency band. *IEEE Transactions on Microwave Theory & Techniques* **60**(3), 845–860.
2. **Kato Y** (2018) Future mobility-enhanced society enabled by semiconductor technology. In *2018 IEEE International Solid-State Circuits Conference - (ISSCC)*, San Francisco, CA, USA, 21–26.
3. **Schwarz D, Riese N, Dorsch I and Waldschmidt C** (2022) System performance of a 79 GHz high-resolution 4D Imaging MIMO radar with 1728 virtual channels. *IEEE Journal of Microwaves* **2**(4), 637–647.
4. **Schwarz D, Dorsch I, Dürr A and Waldschmidt C** (2022) Improving the detection capability of imaging MIMO radars by TX beamforming. In *2022 19th European Radar Conference (EuRAD)*, Milan, Italy, 17–20.
5. **Sadhu B, Gu X and Valdes-Garcia A** (2019) The more (antennas), the merrier: A survey of silicon-based mm-wave phased arrays using multi-IC scaling. *IEEE Microwave Magazine* **20**(12), 32–50.
6. **Lee W** (2019) Fully-integrated 94-GHz dual-polarized TX and RX phased array ICs for 3-D real-time radar imaging applications. In *IEEE/MTT-S International Microwave Symposium (IMS)*, WSL–7.
7. **Mailloux RJ** (2005) *Phased Array Antenna Handbook*, 2nd edn. London: Artech House.
8. **Ku B, Schmalenberg P, Inac O, Gurbuz OD, Lee J, Shiozaki K and Rebeiz GM** (2014) A 77-81-GHz 16-element phased-array receiver with ±50° beam scanning for advanced automotive radars. *IEEE Transactions on Microwave Theory & Techniques* **62**(11), 2823–2832.
9. **Ku B, Inac O, Chang M, Yang H and Rebeiz GM** (2014) A high-linearity 76–85-GHz 16-element 8-transmit/8-receive phased-array chip with high isolation and flip-chip packaging. *IEEE Transactions on Microwave Theory & Techniques* **62**(10), 2337–2356.
10. **Malaquin C** (2022) Market requirements Driving Radar Evolution. In *Automotive forum, European Microwave Week*, Milan, Italy.
11. **Lee JS and Schmalenberg PD** HYBRID RADAR INTEGRATED INTO SINGLE PACKAGE. US patent No. 9116227, 25 August 2015.
12. **Bekers DJ, Jacobs S, Monni S, Bolt RJ, Fortini D, Capece P and Toso G** (2019) A Ka-band spaceborne synthetic aperture radar instrument: A modular sparse array antenna design. *IEEE Antennas and Propagation Magazine* **61**(5), 97–104.
13. **Rocca AP, Mailloux RJ and Toso G** (2015) GA-based optimization of irregular subarray layouts for wideband phased arrays design. *IEEE Antennas and Wireless Propagation Letters* **14**, 131–134.
14. **Rupakula B, Aljuhani AH and Rebeiz GM** (2020) Limited scan-angle phased arrays using randomly grouped subarrays and reduced number of phase shifters. *IEEE Transactions on Antennas and Propagation* **68**(1), 70–80.
15. **Repeta M, Zhai W, Ross T, Ansari K, Tiller S, Pothula HK, Wessel D, Li X, Cai H, Liang D and Wang G** (2020) A scalable 256-element E-band phased-array transceiver for broadband communications. In *2020 IEEE/MTT-S International Microwave Symposium (IMS)*, 833–836.

16. **Vouvakis M** Fundamentals of Phased Arrays. Technical lectures, 81, IMS2020.
17. **Yin Y, Zhang Z, Kanar T, Zihir S and Rebeiz GM** (2020) A 24-29.5 GHz 256-element 5G phased-array with 65.5 dBm peak EIRP and 256-QAM modulation. In *2020 IEEE/MTT-S International Microwave Symposium (IMS)*, 687–690.
18. **Phelps T, Zhang Z and Rebeiz G** (2021) Simultaneous channel phased-array calibration using orthogonal codes and post-coding. In *2021 IEEE MTT-S International Microwave Symposium (IMS)*, 397–399.
19. **Kohtani M, Cha S, Schmalenberg P, Lee J, Li L, Takahata T, Yamaura S, Matsuoka T and Rebeiz G** (2022) Thinned array with steerable nulls to cancel grating lobe for automotive radar applications. In *2022 52nd European Microwave Conference (EuMC)*, Milan, Italy, 385–388.
20. **Sadhu B, Gu X and Valdes-Garcia A** Silicon based millimeter wave phased array design. Technical lectures, IMS2020.

Masato Kohtani received his B.S. and M.S. degrees in electrical engineering from Hokkaido University, Sapporo, Japan, in 1999 and 2001, respectively. In 2001, he joined Sharp Corporation, Osaka, Japan, where he was engaged in the research and development of RF large-scale integrations (LSIs). In 2012, he joined the Samsung R&D Institute Japan, Yokohama, Japan, where he was involved in the development of high data-rate wireless millimeter-wave communication ICs. Since 2014, he has been with DENSO Corporation, Kariya, Japan, and currently with MIRISE Technologies Corporation, Tokyo, Japan. His current research interests include RF and millimeter-wave circuits, built-in self-tests, and phased arrays for radar applications.

Sungwoo Cha received his B.S. and M.S. degrees from Kookmin University, Seoul, Korea, in 1998 and 2001, respectively, and his Ph.D. degree from Osaka University, Osaka, Japan, in 2005. In 2005, he joined Renesas Electronics Corporation, Takasaki, Japan, where he was engaged in research and development of RFICs for 2G to 4G cellular applications. From 2011 to 2013, he was an Industrial Resident of the Research Program in imec, Leuven, Belgium. Since 2015, he has been with DENSO Corporation, Aichi, Japan. From 2018 to 2021, he was loaned to DENSO International America, Inc, San Jose, CA, and he is currently loaned to MIRISE Technologies Corporation, Tokyo, Japan, where he is a Manager of Sensor R&D Division. His research interests include circuit and system design for millimeter-wave automotive radar sensors.

Paul Schmalenberg received his B.Sc. (2006) in electrical engineering from Michigan State University in East Lansing, MI, and his M.Sc. (2012) in electrical engineering with a focus on electromagnetics from University of Michigan in Ann Arbor, MI. He is currently a part of the Toyota Research Institute – North America also in Ann Arbor, MI. His research interests include radar, LIDAR, metamaterials, quantum sensing, and topology optimization.

Jae Seung Lee received his Master and Ph.D degrees from UC Davis, California, in 2004 and 2005, respectively. He is currently a Senior Manager of the Electronics Research Department and Research Strategy Office of Toyota Research Institute of North America in Ann Arbor, Michigan. He has been leading R&D projects of lidar and radar sensors for autonomous driving, power electronics projects for EV charging, energy management, wireless charging, and so on. He now takes responsibility of research strategy and electronics research of Toyota Research Institute of North America. He received 3 'R&D-100 Awards', and he is an author or a co-author of over 50 technical papers and issued over 50 patents.

Linjie Li (Graduate Student Member, IEEE) received his B.Eng. degree in Electronic Information Engineering from Nanjing University of Science and Technology (NJUST), Nanjing, China, in 2019, and his M.S. degree in Electrical Engineering from the University of California at Irvine (UCI), Irvine, USA, in 2021. He is currently pursuing his Ph.D. degree with the Telecommunications and Integrated Antennas, Circuits and Systems Group (TICSG), at the University of California at San Diego (UCSD), La Jolla, USA. His research interests include millimeter-wave antennas and phased-array design for wireless communication systems.

Toshihiko Takahata received his B.S. and M.S. degrees in electrical engineering from Osaka University, Osaka, Japan, in 2002 and 2004, respectively. In 2008, he joined DENSO Corporation, Kariya, Japan, and is currently with MIRISE Technologies Corporation, Aichi, Japan. He is currently engaged in millimeter-wave radar research.

Shinji Yamaura (M05) received his B.E. and M.E. degrees from Tokyo Institute of Technology, Tokyo, Japan, in 1989 and 1991, respectively. In 1991, he joined Fujitsu Laboratories Ltd. Kanagawa, Japan, and was engaged in the research and development of simulation modeling, circuit design, and evaluation technology up to 100 GHz for optical communication systems and wireless communication systems, such as Mobile-WiMAX and CMOS Power Amplifiers for WCDMA/LTE. In 2014, he joined Denso Corporation, Aichi, Japan, and was engaged in millimeter-wave CMOS integrated circuits and mm-wave radar systems. He currently works in the Sensor R&D Division of MIRISE Technologies Corporation. Mr. Yamaura is a member of IEEE SSCS, MTT-S, CAS, APS, SPS, and IEICE of Japan.

Toshihiko Matsuoka received his B.E. and M.E. degrees from the Science University of Tokyo, Japan, in 1992 and 1994, respectively. In 1994, he joined DENSO Aichi, Japan, and was engaged in the development of peripheral circuit design, 32-bit microcontroller and driver-firmware for in-vehicle communication systems, such as CAN/LIN, and dedicated sensor interfaces. He currently works in the Sensor R&D Division of MIRISE Technologies Corporation. His current research interest includes millimeter-wave radar applications.

Gabriel M. Rebeiz is Distinguished Professor, the Wireless Communications Industry Endowed Chair at UCSD, IEEE Fellow and Member of the National Academy. His group has led the development of complex RFICs for phased-array applications from X-band to D-band. He is the father of affordable silicon-based phased-arrays, and his RF-beamforming architectures are used by most companies developing communication and radar phased-arrays. All SATCOM phased-array development is based on his work. Prof. Rebeiz has received the IEEE Microwave Prize three times for his work on phased-arrays, the IEEE MTT Distinguished Educator Award, the IEEE AP John. D. Krauss Award, the IEEE AP Harold A. Wheeler Applications Paper Award, and the IEEE Daniel E. Noble Technical Field Award for his work on RF MEMS. He has graduated 120 PhD students and post-docs, has written more than 850 IEEE publications, and has been referenced over 42,000 times with an h-index of 100. He was a cofounder of Spectra-Beam (acquired by IDT/Renesas), cofounder of Extreme Waves Inc., and is an advisor to several of the large commercial and defense companies in the US.